Erschienen in: Solar Energy Materials and Solar Cells. Elsevier. 2023, 251, 112111
https://doi.org/10.1016/j.solmat.2022.112111

Industrially viable diffused IBC solar cells using APCVD dopant glass layers

Vaibhav V. Kuruganti [a,*], Daniel Wurmbrand [b], Thomas Buck [a], Sven Seren [c], Miro Zeman [d], Olindo Isabella [d], Fabian Geml [b], Heiko Plagwitz [b], Barbara Terheiden [b], Valentin D. Mihailetchi [a]

[a] *International Solar Energy Research Center (ISC) Konstanz, Rudolf-Diesel-Straße 15, 78467, Konstanz, Germany*
[b] *University of Konstanz, Department of Physics, 78457, Konstanz, Germany*
[c] *SCHMID Group, Robert-Bosch-Straße.32-36, 72250, Freudenstadt, Germany*
[d] *Delft University of Technology, PVMD Group, Mekelweg 4, 2628, PH, Delft, Netherlands*

A B S T R A C T

Even though interdigitated back contact (IBC) architecture produces the most efficient solar cells, it is difficult to make them cost-effective and industrially viable. Therefore, single-sided atmospheric pressure chemical vapor deposition (APCVD) is investigated for the fabrication of IBC solar cells because it reduces the overall thermal budget, simplifies wet bench processing, and requires no additional masking layer. For the fabrication of a full APCVD IBC solar cell, a very lightly doped front surface field (FSF) of 650 Ω/sq, a heavier doped back surface field (BSF) of 100 Ω/sq and a moderately doped emitter of 250 Ω/sq was used. The high-temperature annealing step is partially done in an oxygen (O_2) environment to (i) drive in dopants, (ii) prevent the formation of a boron-rich layer in case of p^+ doped c-Si, and (iii) grow an in-situ SiO_2 at the Si/dopant glass interface. The etch rate difference between the in-situ grown SiO_2 and the doped glass layer is utilized to etch the doped glass completely. The retained in-situ SiO_2 after etching is capped with plasma-enhanced chemical vapor deposited (PECVD) SiN_x for the passivation of both polarities of IBC solar cells. A full APCVD IBC solar cell precursors (i.e. before metallization) obtained implied open-circuit voltage (iV_{oc}) of 714 mV and emitter saturation current density (J_{0s}) of 17 fA/cm^2. At the device level, a full APCVD IBC solar cell achieved a conversion efficiency of 22.8% with V_{oc} of 696 mV and short-circuit current density J_{SC} of 41.3 mA/cm^2. These parameters are comparable to the commercially available full-tube diffused ZEBRA® IBC solar cells.

1. Introduction

In the early 1950s, the first silicon solar cells were fabricated on an n-type substrate using an interdigitated back contact (IBC) architecture [1]. IBC solar cells are the optimal choice for fabricating high-efficiency solar cells since all metallization can be placed on the non-illuminated side of the solar cells, enhancing the incident light absorption on the front side [2]. Other benefits of IBC architecture include lower series resistance due to a higher metal fraction, simple module integration, and its potential in building integrated photovoltaics (BIPV) due to the module's visually pleasant look [3]. Silicon heterojunction (SHJ) technology has enabled crystalline silicon (c-Si) solar cells with an IBC configuration to achieve a world-record conversion efficiency of 26.7% (designated area: 180 cm^2) [4]. Sunpower Corporation, the most successful company commercially manufacturing large area passivating contacts IBC solar cells, have reported efficiencies of 25.2% [5]. Lastly, the ISC Konstanz-developed ZEBRA® technology is a bifacial IBC solar cell concept based on a typical industrial low-cost manufacturing method that has exhibited mass production efficiencies surpassing 23.5% [6].

IBC architectural cell technologies are still a niche industry due to their intricate processing sequence and expensive production costs [7]. First, because of the inherent nature of the IBC architecture, the rear side must be patterned using photolithography [8,9], inkjet patterning [10] or a laser process [11,12] in conjunction with multiple wet bench cleaning processes. Secondly, since all charge carriers need to be collected on the rear side, the wafer bulk should have a high minority carrier lifetime. Thirdly, the fabrication of the three different doped regions, the so-called FSF or front floating emitter (FFE), the BSF, and the emitter would necessitate multiple high-temperature steps that would significantly increase the thermal budget and process complexity. Finally, passivation of IBC architecture is cumbersome as locally doped opposite polarities are located at the rear side and hence would require a universal passivation stack for both polarities. In this study, using laser technology and high-quality n-type substrate materials, the latter two constraints are addressed for fabricating industrially viable IBC solar cells [13].

Using doped glass layers based on atmospheric pressure chemical vapor deposition (APCVD) [14] instead of conventional gas tube diffusion, where the doped glass is grown and driven in, would decrease the

* Corresponding author.
E-mail address: vaibhav.kuruganti@isc-konstanz.de (V.V. Kuruganti).

Konstanzer Online-Publikations-System (KOPS)
URL: http://nbn-resolving.de/urn:nbn:de:bsz:352-2-1w7prvhu9wbvn0

process complexity of IBC solar cells. Additionally, APCVD dopant glass layers are deposited before diffusion; therefore, little or no spacing is required in the diffusion furnace, which can significantly increase throughput [15]. Furthermore, by using APCVD layers, we can decouple the deposition step from the diffusion step, allowing us to perform laser processing steps before a high-temperature step or co-annealing to reduce the overall thermal budget [16,17]. Some other advantages of APCVD processing include lower operational and maintenance costs and high throughput [18].

This study investigated the effect of varying APCVD dopant concentrations on layers' electrical properties after high-temperature annealing. The annealing recipe was optimized for three purposes, namely: drive in the dopants, prevent boron-rich layer (BRL) [19] formation in case of p^+ doped c-Si, and grow an in-situ SiO_2 at the interface between glass and Si for passivation purpose [20]. Furthermore, the in-situ grown SiO_2 at the interface serves as an etch barrier for the controlled etch back of APCVD borosilicate glass (BSG) and phosphosilicate glass (PSG) layers with varying dopant concentrations in a single wet bench HF glass removal step. The passivation quality was measured on symmetrical lifetime samples and solar cell precursors with a SiO_2/SiN_x passivation stack. Finally, all learnings were integrated for a streamlined and cost-effective approach to fabricating high-efficiency APCVD IBC solar cells.

2. Experimental

2.1. Sheet resistance and symmetrical lifetime samples preparation

For our sheet resistance (R_{SH}) samples, we used pseudo-square 180 ± 10 µm thick M2 Czochralski (Cz) wafers with opposite doping to that of doped layers to investigate, that is, n-type Cz-Si wafers with base resistivity $\rho_B = 3\ \Omega$ cm and p-type Cz-Si wafers with base resistivity $\rho_B = 0.95\ \Omega$ cm. All samples underwent an alkaline etch to remove saw-cutting-induced damages, followed by a piranha cleaning process to remove organic and inorganic impurities before the APCVD dopant glass deposition. The APCVD equipment is a SCHMID APCVD Roller-Transport System with multiple deposition chambers enabling more than one layer in a single pass. The layers of borosilicate glass (BSG) and phosphosilicate glass (PSG) were 40 nm thick. In addition, to prevent the doped layers underneath from reacting with the environment [21], an additional 20 nm thick undoped silicate glass (USG) capping layer was deposited. Finally, the doped glass layers were annealed in a partial O_2 environment to form the p^+ and n^+ doped regions. The glass layers on top of c-Si were etched in an HF solution to measure the doped regions' electrical properties. R_{SH} was measured using the four-point probe tool from GP Solar, and the active dopant profile was determined using an electrochemical capacitance-voltage (ECV) tool from WEP.

For our symmetrical lifetime samples, we used only n-type Cz-Si wafers with base resistivity $\rho_B = 3\ \Omega$ cm and nominal thickness of 180 ± 10 µm. The processing sequence of symmetrical lifetime samples was similar to that of the above-mentioned R_{SH} samples until the high-temperature annealing step, except that both sides of the wafer had the same dopant glass layer deposited. Then, the in-situ grown SiO_2 is used as a buffer layer to completely etch the APCVD dopant glass layer. A detailed description of this systematic etching procedure using SiO_2 as a buffer layer can be found in Ref. [20]. Finally, on both sides, these samples received 75 nm thick plasma-enhanced chemical vapor deposition (PECVD) SiN_x. Then, the samples were fired in a belt-type rapid-firing furnace for hydrogenation using our best-known in-house settings [22]. For measuring the iV_{oc} and J_{0s} of the doped regions, we have used a WCT-120 lifetime tester from Sinton instruments. For the QSSPC measurements, we have used a base resistivity of $\rho_B = 3\ \Omega$ cm and thickness t of 170 µm. For the flat passivated symmetrical lifetime samples, an optical constant of 0.95 was selected, whereas an optical constant of 1.1 was chosen for the passivated textured solar cell precursor samples.

2.2. Complete APCVD IBC solar cells

Fig. 1 indicates the schematic fabrication process and corresponding structure of the full APCVD IBC solar cell. The substrate is Cz-Si M2 wafers with a base resistivity of $\rho_B = 3\ \Omega$ cm and a thickness of 180 ± 10 µm. First, all samples underwent alkaline etching to remove the saw-cutting-induced damage, followed by the piranha cleaning process. An APCVD BSG layer was deposited on the rear side of the wafers and subsequently annealed in an O_2 environment to form the emitter region. The samples then received a PECVD SiN_x masking layer on the rear side. After laser patterning, the rear side of the wafers was alkaline etched and cleaned. An APCVD PSG layer with a low doping concentration was deposited on the front side, and a high doping concentration was deposited on the rear side and subsequently annealed in an O_2 environment to form the BSF region on the rear and the FSF region on the front side of the substrate. Similarly to lifetime samples, the in-situ grown SiO_2 was used as a buffer layer to completely etch the APCVD BSG and PSG layers after annealing. For passivation purposes, both sides received a PECVD SiN_x layer. The metallization of these samples was achieved using our best-known method of screen printing and firing through the process from ZEBRA® technology [22].

To investigate the passivation quality of the solar cell before metallization, we have also fabricated solar cell precursors. It is essential to account for numerous artefacts that might induce an overestimation of the carrier lifetime when interpreting photoconductance-based lifetime measurements. One such scenario involves samples with a conductive layer disrupted by lines of opposing polarity doping, resulting in laterally alternating p^+/n^+ doping areas [23]. This structure often appears in the emitter region of samples that monitor the lifetime of interdigitated back contact cells. To avoid overestimating passivation quality, the processing sequence for the solar cell precursor samples follows that shown in Fig. 1(a), except for the PECVD masking, laser patterning processes and rear side PSG deposition. As such, the final structure of the solar cell precursor samples has a full area emitter on the flat rear and a full area FSF on the textured front side.

To compare our novel full APCVD IBC solar cells and solar cell precursors, we have fabricated three groups: full tube diffused, hybrid-1 and hybrid-2. The doped regions (i.e. BSF, FSF and emitter) in all these solar cell concepts are formed by either annealing the APCVD glass layer or using the standard industrial tube diffusion. Table 1 summarizes how the doped regions in different solar cell groups were fabricated. In addition, the full tube diffused precursor cells are manufactured using the ZEBRA best-known method and are used here as a process reference.

3. Results and discussion

3.1. Electrical properties of the doped regions

The electrical properties of the doped regions were analyzed using sheet resistance samples specified in the experimental section. This study investigated the electrical characteristics of annealed APCVD BSG and PSG with three different dopant concentrations. The minimum and maximum temperatures in the annealing recipe were 810 °C and 995 °C, respectively. At the peak temperature of 995 °C, annealing was done in a 100% O_2 environment. The presence of APCVD BSG or PSG layers on the silicon surface offers almost no hindrance for the O_2 reaching the Si surface because of the high diffusivity of O_2 in doped glass layers compared to pure SiO_2 [24]. Similar studies were carried out by Mihailetchi et al. [20], where the BSG layer grown from the tube-diffused BBr_3 offered little resistance for the oxygen to diffuse to the silicon interface. Also, Mihailetchi et al. [20] demonstrated that irrespective of the BSG thickness uniformity across the wafer or along the diffusion boat, the in-situ grown thermal SiO_2 was very homogeneous, making it an attractive option for being used as passivation and ARC layers. Moreover, boron has a higher segregation coefficient in SiO_2 than Si [25]. Hence the post-oxidation ensures that the higher

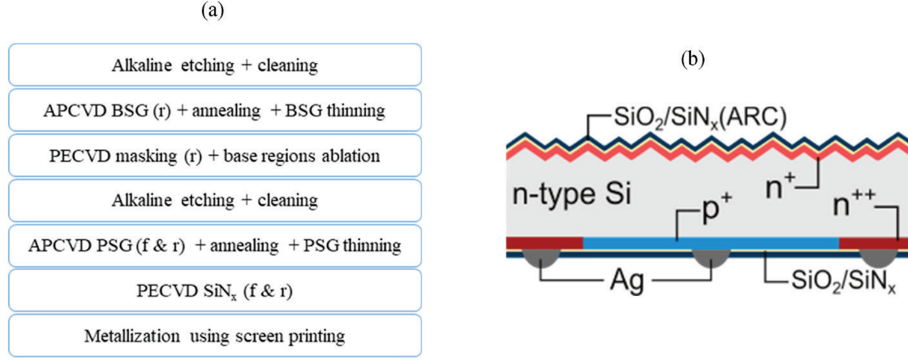

Fig. 1. Main process steps to fabricate the full APCVD IBC solar cell (a) and a schematic cross-section view of the resulting IBC cell (b).

Table 1
Different techniques for forming the doped regions and their corresponding R_{SH} values of the four IBC solar cell types investigated in this paper.

Solar cell group	FSF (n^+)	BSF (n^{++})	Emitter (p^+)
Full APCVD R_{SH} (Ω/sq)	APCVD PSG 650 Ω/sq	APCVD PSG 100 Ω/sq	APCVD BSG 250 Ω/sq
Hybrid-1 R_{SH} (Ω/sq)	$POCl_3$ diffusion 150 Ω/sq	$POCl_3$ diffusion 80 Ω/sq	APCVD BSG 250 Ω/sq
Hybrid-2 R_{SH} (Ω/sq)	APCVD PSG 650 Ω/sq	APCVD PSG 100 Ω/sq	BBr_3 diffusion 150 Ω/sq
Full tube diffused Reference: ZEBRA® [6]	$POCl_3$ diffusion	$POCl_3$ diffusion	BBr_3 diffusion

concentration of boron at the surface segregates into the SiO_2, thereby preventing the formation of BRL, which has proven to degrade bulk lifetime and cause very high emitter saturation current densities [26].

Fig. 2(a) shows the R_{SH} data of the boron and phosphorous-doped regions after annealing as a function of the APCVD glass dopant concentration. With increasing dopant concentration, we observe a decrease in R_{SH} for both polarities and an increase in the homogeneity of the R_{SH}. For the operating temperatures (810 °C and 1100 °C) used in this study, activation energies of phosphorous and boron are 2.74 ± 0.007 eV and 3.12 ± 0.004 eV, respectively [27]. Hence, for a similar dopant concentration of 8.0 wt %, we observe higher doping of phosphorous (80 Ω/sq) compared to boron (320 Ω/sq).

When selecting the electrical properties of the p^+ and n^+ regions on the rear side of IBC solar cells, three crucial parameters, i.e. J_{0pass}, J_{0met}, and ρ_c, should be minimized to increase the cell efficiency [28]. Here, the knowledge gained from our tube-diffused ZEBRA IBC technology was used to select optimal electrical properties of emitter and BSF for APCVD IBC solar cells [22]. Accordingly, a 250 Ω/sq emitter and 100 Ω/sq BSF were selected. Due to the flexibility of single-sided APCVD deposition technology, we chose a very lightly doped FSF (650 Ω/sq) in this study. Fig. 2(b) shows the carrier concentration profiles of the shortlisted layers. The low surface concentrations of 9.5×10^{18} cm^{-3} for the p^+ emitter layer show that the annealing in an oxygen environment has successfully prevented the formation of BRL. Also, very lightly doped FSF with R_{SH} of 650 Ω/sq and a surface concentration of 2.5×10^{18} cm^{-3} with a shallow junction depth of 0.18 μm was used in this work. Since there is no need for any metallization at the front side of the IBC solar cells, having a very lightly doped front surface field can be well passivated, reducing the surface recombination while augmenting the spectral response in the ultraviolet range (280 nm–400 nm) and thus improving the V_{OC} and J_{SC} [29].

3.2. Etch rate study of silicon dioxide/doped oxide glass stack

During the high-temperature annealing step, apart from driving dopants into the bulk, we grow a homogeneous SiO_2 of 32 nm at the doped glass/Si interface. In this section, we show that the in-situ grown thermal SiO_2 can be used as a buffer layer due to the difference in the etching rate of doped glass layers compared to thermally grown SiO_2. In the following section, we show that the partially etched back SiO_2, when capped with PECVD SiN_x, offers excellent surface passivation for both p^+ and n^+ doped regions, thereby acting as a universal passivation scheme with fewer processing steps in IBC solar cell concepts.

To investigate the etch rate of different layers, the wafers were immersed in 2-vol% HF acid solution for a defined period, followed by thickness measurement. The thickness of BSG, PSG and SiO_2 were measured using a Sentech SE-800PV ellipsometer, assuming the refractive index of $n = 1.46$ for all glass layers [30].

Fig. 3(a) shows the thickness variation across the wafer at different processing stages of the samples. During the as-deposited stage, we

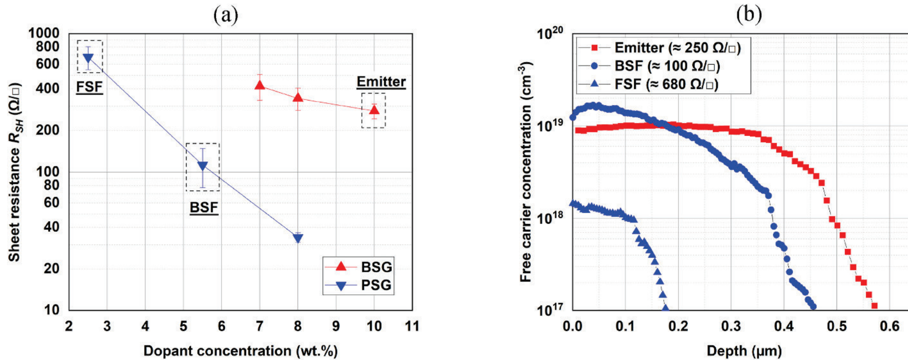

Fig. 2. (a) Sheet resistance R_{SH} after high-temperature annealing of APCVD layers with different dopant concentrations and dopant types. (b) Carrier concentration profiles of the p^+ doped emitter layer, lightly doped n^+ FSF layer and heavily doped n^{++} BSF layer used in the full APCVD IBC cell process.

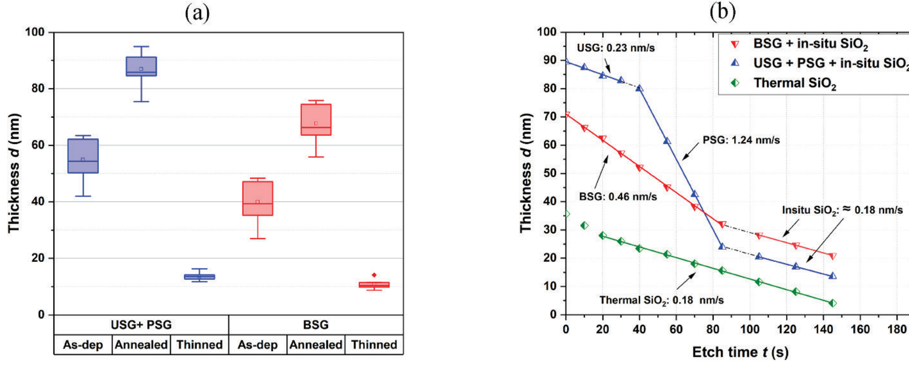

Fig. 3. (a) Thickness of the USG + PSG layer stack and BSG layer measured after APCVD deposition, directly after annealing the samples in an O_2 environment, and after HF thinning. (b) The thickness of the different annealed oxide stacks (see legend) used in this study as a function of etching time in 2-vol% HF solution. The arrows represent the etching rates of the different layers within the stack. To compare the etching rate of the in-situ grown SiO_2, a reference samples with 32 nm of thermally grown SiO_2 was used in this study.

deposit 40 ± 7.2 nm of BSG and 60 ± 7.7 nm of PSG + USG layer. We observe a high inhomogeneity of thickness across the wafer. Upon annealing these layers in the O_2 atmosphere, we grow a 32 nm thick uniform in-situ SiO_2 layer at the interface of c-Si and the dopant glass. Upon thinning the layer stack in HF solution, the dopant glass layer is etched completely, and a 13.6 ± 1.4 nm (in case of USG + PSG) and 11.2 ± 1.4 nm (in case of BSG) in-situ grown SiO_2 layer remains on Si surface, which served as a passivation layer. The significant improvement in thickness uniformity across the wafer, as measured by the standard deviation value after thinning in HF, is attributable to the slower etching of in-situ grown SiO_2 compared to dopant glass layers.

Fig. 3(b) depicts the thickness of the different layers stacks as a function of etching time in 2-vol% HF solution. As indicated by the arrows, the etching rate of each layer was calculated using the slope of thickness versus etching time. The green rhombus represents the thermally grown SiO_2, which was used as a reference to compare the etching rates of the in-situ grown SiO_2 after annealing in an O_2 environment; the inverted red triangle represents the annealed "APCVD BSG + in-situ grown SiO_2" stack, and the blue triangles represent the "APCVD USG + PSG + in-situ grown SiO_2" stack. The USG capping layer was necessary to protect the otherwise hygroscopic PSG layer [21].

The wafers were immersed in the 2-vol%HF solution, followed by the immersion in deionized water, to stop the etching process. Uncertainty in estimating the etching rate could arise due to the unintended slow etching during the transportation of the wafers from the HF solution beaker to the DI water beaker. Due to the short etching times, the relative measurement error of the etching rate is approximately 15%. The etching rate of thermally grown SiO_2 was determined to be 0.18 ± 0.02 nm/s, equivalent to Spierings et al. [31] at an HF concentration of 2 wt%. The stack etch rate findings for co-annealed "APCVD BSG + in-situ grown SiO_2" were separated into the BSG zone and the in-situ grown SiO_2 zone. Like Mihailetchi et al. [20], the BSG layer exhibited a much higher etching rate of 0.46 nm/s than thermally produced SiO_2 (0.18 nm/s). The difference in etching rate is because the breaking rate of B–O bonds in HF solution is significantly higher than that of Si–O bonds [32]. After 100 s of etching in HF solution, we have already reached the in-situ grown SiO_2 regime, and the etching rate drops by almost 2.5. In this zone, we see the etching rate being equal to that of thermal SiO_2 (blues triangles), pointing out that the properties of the in-situ grown oxide are comparable to that of the thermally grown oxide without any dopant layer on top. Finally, etch rate findings for the co-annealed "APCVD USG + PSG + in-situ grown SiO_2" stack was separated into three regimes: USG capping zone, PSG zone, and in-situ SiO_2 zone: USG capping zone, PSG zone and in-situ SiO_2 zone. The etching rate of the APCVD annealed USG layer is determined to be 0.24 ± 0.03 nm/s which is marginally higher than that of thermally grown SiO_2. The observed disparity in etching speeds can be due to CVD and thermal oxides' different compositions and porosities [32]. The APCVD PSG layer exhibited the maximum etching rate in this investigation, with an etching rate as high as 1.24 ± 0.12 nm/s, which is over 7.7 times greater than thermally produced SiO_2. Hence, it can be said that the breakage rate of P–O bonds in HF solution is faster than (>) B–O bonds, which in turn exceeds that of > Si–O bonds. After 100 s of HF etching, we enter the third phase of the in-situ SiO_2 and see similar behavior to that of the annealed BSG stack. Hence, we have demonstrated that by using a single HF etching step (in this case of 145 s) for our annealed doped glass layers, we can completely get rid of both BSG and PSG by using their selective etching compared to in-situ grown SiO_2 in HF solution. Mojrova et al. [33] have demonstrated that for the optimal passivation quality of the SiO_2/SiN_x passivation stack, we need at least 10 nm of the SiO_2 and a SiN_x layer with a low refractive index. Hence in this work, the etching time was adjusted such that at least 10 nm of the in-situ grown silicon oxide remained on the doped c-Si surface. This partly etched-back SiO_2 is subsequently covered with PECVD SiN_x to passivate both polarities of the IBC solar cells.

4. Passivation quality and IV results at the device level

As described in the experimental section, Symmetrical lifetime samples were used to study the passivation quality of the doped APCVD layers. Fig. 4(a) shows the iV_{oc} and J_{0s} of the doped regions, whereas Fig. 4(b) shows their corresponding injection-dependent lifetime results. Table 2 shows the individual saturation current density (J_0) contributions and iV_{oc} of the symmetrical lifetime structures and the solar cell precursor groups. The J_{0s} contribution was extracted at an injection level of 5×10^{15} cm^{-3} using the Kane and Swanson method [34]. The measured J_{0s} values displayed in Fig. 4 (a) and 4(c) and Table 2 indicate the J_0 contributions from both sides of the doped regions. At one sun illumination, since the effective lifetime (τ_{eff}) and J_{0s} of the doped region can be measured, bulk lifetime (τ_{bulk}) can be calculated using equation (1), and subsequently, the saturation current density of the bulk region (J_{0b}) can be calculated using equation (2). Finally, the Overall saturation current density (J_{0t}) was found by summing up J_{0b} and J_{0s}. Here N_{dop} is the background dopant density, W is the thickness of the samples, Δn is the injection level at one-sun condition, and n_i is the intrinsic carrier concentration of silicon.

$$\frac{1}{\tau_{eff}} = \frac{1}{\tau_{bulk}} + \frac{J_{0s}\left(N_{dop} + \Delta n\right)}{q \times n_i^2 \times W} \tag{1}$$

$$J_{0b} = \frac{q \times n_i^2 \times W}{N_{dop} \times \tau_{bulk}} \tag{2}$$

FSF and BSF layers have iV_{oc} values above 690 mV, whereas the emitter layer has a much lower $iV_{oc,}$ around 675 mV. A lower J_{0b} of n^+ doped areas is attributable to the enhanced gettering efficacy of APCVD PSG compared to APCVD BSG at the same annealing temperature [16]. Secondly, the lightly doped FSF layer has higher iV_{oc} and lower J_{0s} than the heavily doped BSF layer. We estimated the influence of Auger recombination on the J_{0s} values of the BSF and FSF-doped areas using EDNA 2 [35]. The overall two sides Auger recombination contribution

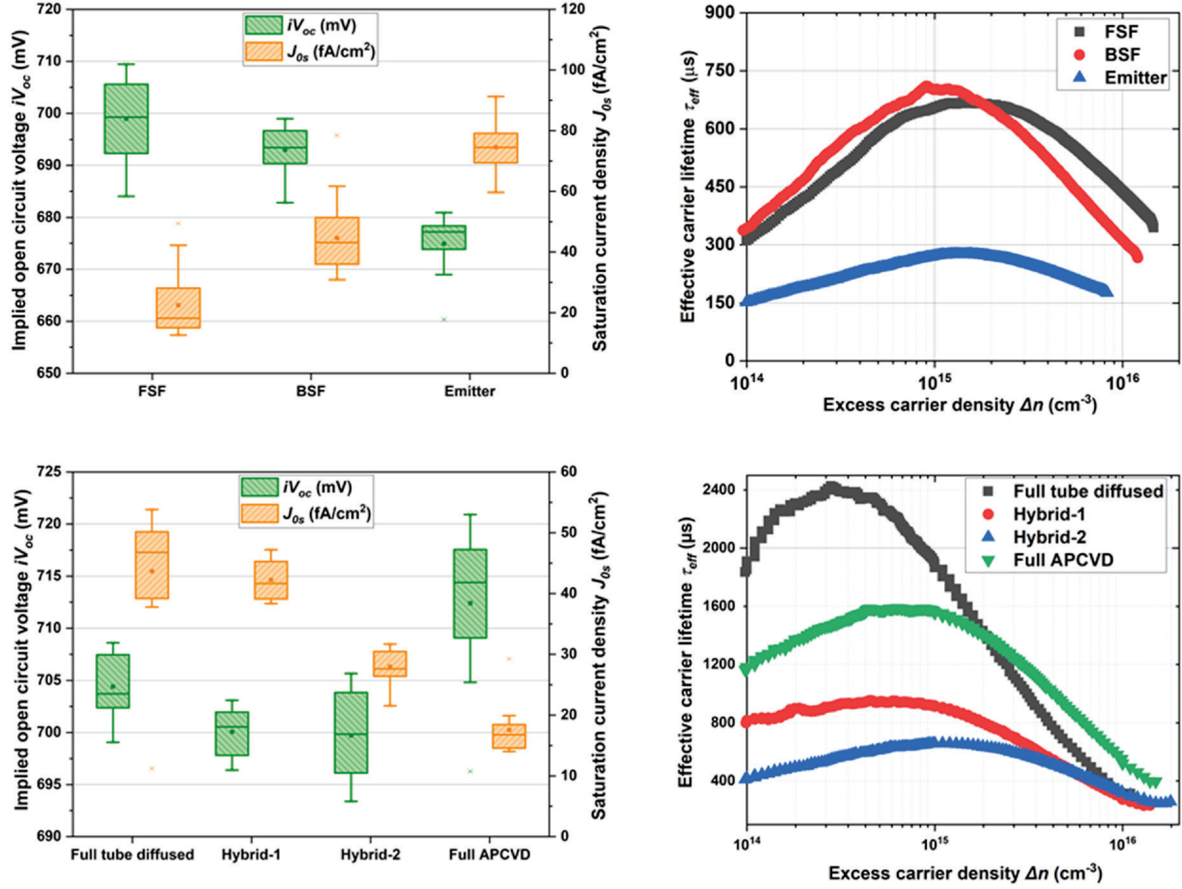

Fig. 4. (a) iV_{oc} and J_{0s} of symmetrical FSF (n^+), BSF (n^{++}) and emitter (p^+) lifetime samples formed by annealing of APCVD layers. (b) Injection-dependent lifetime results of the symmetrical lifetime samples. (c) iV_{oc} and J_{0s} of solar cell precursor as follows: Full tube diffused, hybrid-1, hybrid-2 and full APCVD solar cells precursors. (d) Injection-dependent lifetime results of the different solar cell precursors.

Table 2
Average individual J_0 contributions due to recombination in the wafer bulk J_{0b}, doped regions (including Auger) surface J_{0s}, and their corresponding average iV_{oc} values. The J_{0t} is the total saturation current density of symmetrical lifetime samples or solar cell precursors estimated by adding the relevant individual contributions.

Group	Sample structure	J_{0b} (fA/cm^2)	J_{0s} (fA/cm^2)	J_{0t} (fA/cm^2)	iV_{oc} (mV)
Emitter	Lifetime	50	72	122	679
BSF	Lifetime	25	45	70	692
FSF	Lifetime	33	17	51	702
Full tube diffused	Precursor	5	42	47	706
Hybrid-1	Precursor	21	42	63	698
Hybrid-2	Precursor	39	29	68	696
Full APCVD	Precursor	19	17	36	712

Table 3
Parameters of the best solar cells extracted from current-voltage characteristics of the different groups of solar cells as mentioned in Table 3, namely: Full tube diffused cells (ref.), hybrid-1 cells, hybrid-2 cells and Full APCVD cells.

Group	J_{sc} (mA/cm^2)	V_{oc} (mV)	FF (%)	η (%)
Full tube diffused (ref.)	41.3	690	80.0	22.8
Hybrid-1	40.7	686	78.3	21.9
Hybrid-2	41.3	693	79.1	22.6
Full APCVD	41.3	696	79.3	22.8

for the weakly doped FSF region is just 0.6 fA/cm^2 compared to 25 fA/cm^2 for the BSF region. Hence, the observed difference in J_{0s} is attributed mainly to the difference in their Auger recombination.

The passivation quality of the four solar cell precursor groups (i.e. before metallization) and their corresponding injection-dependent lifetime curves are depicted in Fig. 4(c) and (d), respectively. As a reference group, full-tube diffused precursors had a mean iV_{oc} of 704 mV and a mean J_{0s} of 47 fA/cm^2, respectively. Despite having the highest J_{0s} in the group, the full tube diffusion precursor gives the second-best iV_{oc}. As evidenced by the injection-dependent lifetime curves (Fig. 4(d)) at lower injection levels and from the estimated J_{0b} in Table 1, $POCl_3$ and BBr_3 tube diffusions were highly effective in gettering the bulk layer, hence enhancing the iV_{oc} of this cell precursor group. In Fig. 4(c), hybrid-1 and hybrid-2 precursor cells displayed comparable iV_{oc} but distinguishable J_{0s}. Lower J_{0s} seen in the hybrid-2 precursor result from the lightly doped FSF (680 Ω/sq) created by annealing the APCVD PSG as opposed to the heavily doped FSF (150 Ω/sq) formed via $POCl_3$ tube diffusion in the hybrid-1 precursor. Due to the improved gettering efficiency of $POCl_3$ diffusion (also found in full diffused precursors) in hybrid-1 precursors, the J_{0t} of both hybrid precursors is comparable, which explains their comparable iV_{oc}.

Complete APCVD precursors have shown the best passivation quality among all the groups, with mean iV_{oc} of 714 mV and J_{0s} as low as 17 fA/cm^2. Such high passivation quality is generally observed in solar cells endowed with carrier-selective junctions [33,34]. The excellent passivation quality of complete APCVD precursors is attributed to the high quality of the APCVD dopant glasses, the difference in electrical properties such as sheet resistance and surface dopant concentrations, and the difference in sample preparation and the optimized

high-temperature annealing steps. Compared to the symmetrical lifetime samples, the higher iV_{oc} is due to improved gettering of the bulk layer during the second high-temperature annealing, as shown by the J_{0b} values in Table 1. Combining the J_{0s} contributions from the single-sided emitter and FSF yields a J_{0s} of 45 fA/cm^2, whereas the J_{0s} measured for the full APCVD precursor (which is formed by single-sided emitter on the rear and FSF on the front) was considerably lower. This observed discrepancy is unknown and needs deeper investigation. However, we suspect it to be caused by a combination of the three factors: 1) The second high-temperature annealing process, which might getter the emitter layer; 2) Additional hydrogenation from the PECVD capping SiN_x layer, which was deposited for masking and patterning purposes, and 3) Higher number of cleaning steps. As a result, to achieve a J_{0s} of 17 fA/cm^2 in solar cell precursor, the J_{0s} on the emitter layer should also be about 17 fA/cm^2. Nevertheless, J_{0s} values of the emitter in the full APCVD precursor reported in this work were comparable and in good agreement with literature-reported values of SiO_2/SiN_x-based passivation methods commonly used in the industry for the passivation of p^+ regions of solar cells [20,36].

Table 2 presents the solar cell performance parameters of the best solar cells extracted from current-voltage characteristics of the different groups of solar cells studied in this work. The J_{sc} of the hybrid-1 solar cells was 0.6 mA/cm^2 lower than hybrid-2 solar cells. The spectral response measurements (data not shown) showed lower internal quantum efficiency response in the UV region (280 nm–400 nm) caused by the higher doping of the FSF layer in hybrid-1 compared to hybrid-2 solar cells. The full tube diffused (ref.) IBC solar cells and full APCVD IBC solar cells have comparable conversion efficiencies. In the case of full APCVD IBC solar cells, even after having a very lightly doped FSF on the front side, we obtain a similar J_{sc} and a boost of 6 mV in V_{oc} compared to the full tube diffused IBC solar cells, as also observed with the solar cell precursors. The lower *FF* observed in full APCVD IBC solar cells is attributed to the higher sheet resistance of the emitter layer in comparison to full tube diffused IBC solar cells ($R_{SH} = 150\ \Omega$/sq). By further optimizing the APCVD dopant concentration of the emitter layer and fine-tuning of high-temperature annealing step, obtaining efficiencies exceeding 23% is feasible.

5. Summary

This paper presents a systematic study using the APCVD technology for the low-cost fabrication of high-efficiency IBC solar cells. We have demonstrated that a full APCVD-based IBC solar cell flowchart can produce similar power conversion efficiencies as those based on commercially available ZEBRA® [6], which is fabricated using industry-standard BBr_3 and $POCl_3$ tube diffusion systems.

We have investigated the influence of APCVD dopant concentrations on the electrical properties of the doped regions. The annealing recipe chosen in this study had three primary purposes: drive-in of dopants into the substrate, growth of a thermal SiO_2 at the silicon glass interface for passivation purposes, and preventing the formation of a BRL. Based on the electrical properties after annealing the individual APCVD glass layers (i.e. R_{SH} and J_{0s}), a 250 Ω/sq emitter, 100 Ω/sq BSF and 650 Ω/sq FSF were chosen for the fabrication of the full APCVD IBC solar cells. We show that the in-situ grown thermal SiO_2 formed during the annealing in a partial O_2 environment can be used as a buffer layer to etch back partially or entirely the APCVD PSG or BSG in a single HF wet bench step. The remaining in-situ oxide, when capped with PECVD SiN_x, gave excellent surface passivation on both p^+ and n^+ doped regions. On full APCVD solar cell precursors (i.e., without metallization), we obtained an iV_{oc} of 714 mV and a J_{0s} as low as 17 fA/cm^2, which are outstanding values for diffused junctions. At the device level, for metallized large-area IBC cells, we have demonstrated conversion efficiencies approaching 23% for a process entirely based on the APCVD-doped glass deposition technique.

CRediT authorship contribution statement

Vaibhav V. Kuruganti: Writing – original draft, Visualization, Methodology, Investigation, Conceptualization. **Daniel Wurmbrand:** Writing – review & editing, Resources, Conceptualization. **Thomas Buck:** Writing – review & editing, Supervision. **Sven Seren:** Writing – review & editing, Project administration. **Miro Zeman:** Writing – review & editing, Supervision. **Olindo Isabella:** Writing – review & editing, Supervision. **Fabian Geml:** Writing – review & editing, Resources. **Heiko Plagwitz:** Writing – review & editing, Resources. **Barbara Terheiden:** Writing – review & editing, Project administration. **Valentin D. Mihailetchi:** Writing – review & editing, Supervision, Project administration, Conceptualization.

Declaration of competing interest

The authors declare that they have no known competing financial interests or personal relationships that could have appeared to influence the work reported in this paper.

Data availability

Data will be made available on request.

Acknowledgements

This work is supported by the BMWi within the research project "RALPH" (contract no. 03EE1018C)

References

[1] D.M. Chapin, C.S. Fuller, G.L. Pearson, A new silicon p-n junction photocell for converting solar radiation into electrical power [3], J. Appl. Phys. 25 (5) (1954) 676–677, https://doi.org/10.1063/1.1721711.
[2] M.D. Lammert, R.J. Schwartz, The interdigitated back contact solar cell: a silicon solar cell for use in concentrated sunlight, IEEE Trans. Electron. Dev. 24 (4) (1977) 337–342, https://doi.org/10.1109/T-ED.1977.18738.
[3] P. Verlinden, F. Van de Wiele, G. Stehelin, J.P. David, An interdigitated back contact solar cell with high efficiency under concentrated sunlight, in: In Seventh E.C. Photovoltaic Solar Energy Conference, Springer, Dordrecht, 1987, pp. 885–889.
[4] K. Yoshikawa, et al., Exceeding conversion efficiency of 26% by heterojunction interdigitated back contact solar cell with thin film Si technology, Sol. Energy Mater. Sol. Cells 173 (2017) 37–42, https://doi.org/10.1016/j.solmat.2017.06.024. June.
[5] D.D. Smith, G. Reich, M. Baldrias, M. Reich, N. Boitnott, G. Bunea, Silicon solar cells with total area efficiency above 25, Conf. Rec. IEEE Photovolt. Spec. Conf. (2016-November) 3351–3355, https://doi.org/10.1109/PVSC.2016.7750287. Nov. 2016.
[6] R. Kopecek, et al., ZEBRA Technology: Low Cost Bifacial IBC Solar Cells in Mass Production with Efficiency Exceeding 23.5%, Jan. 2021, pp. 1008–1012, https://doi.org/10.1109/pvsc45281.2020.9300503.
[7] G.M. Wilson, et al., The 2020 photovoltaic technologies roadmap, J. Phys. D Appl. Phys. 53 (49) (2020), https://doi.org/10.1088/1361-6463/ab9c6a.
[8] F. Feldmann, et al., Industrial TOPCon solar cells realised by a PECVD tube process, *37th* Eur. Photovolt. Sol. Energy Conf. Exhib. (2018) 164–169.
[9] R.A. Sinton, Simplified backside-contact solar cells, Conf. Rec. IEEE Photovolt. Spec. Conf. 37 (2) (1990).
[10] A.J. Lennon, A.W.Y. Ho-Baillie, S.R. Wenham, Direct patterned etching of silicon dioxide and silicon nitride dielectric layers by inkjet printing, Sol. Energy Mater. Sol. Cells 93 (10) (2009) 1865–1874, https://doi.org/10.1016/j.solmat.2009.06.028.
[11] J. Libal, et al., The zebra cell concept - large area n-type interdigitated back contact solar cells and one-cell modules fabricated using standard industrial processing equipment, 27th Eur. Photovolt. Sol. Energy Conf. Exhib. (Oct. 2012) 567–570, https://doi.org/10.4229/27THEUPVSEC2012-2AO.2.1, no. 3-936338-28–0.
[12] M. Dahlinger, B. Bazer-Bachi, T.C. Röder, J.R. Köhler, R. Zapf-Gottwick, J. H. Werner, 22.0% Efficient laser doped back contact solar cells, Energy Proc. 38 (2013) 250–253, https://doi.org/10.1016/j.egypro.2013.07.274.
[13] P.J. Verlinden, et al., Pilot production of 6" IBC solar cells yielding a median efficiency of 23% with a low-cost industrial process, *32nd* Eur. Photovolt. Sol. Energy Conf. Exhib. (Jul. 2016) 571–574, https://doi.org/10.4229/EUPVSEC20162016-2DO.16.3.
[14] P. Rothhardt, C. Demberger, A. Wolf, D. Biro, Co-diffusion from APCVD BSG and POCl3 for industrial n-type solar cells, Energy Proc. 38 (2013) 305–311, https://doi.org/10.1016/j.egypro.2013.07.282.

[15] J. Fichtner, A. Zuschlag, G. Hahn, Gettering efficacy of diffusion processes based on doped APCVD glasses, AIP Conf. Proc. 1999 (August 2018), https://doi.org/10.1063/1.5049322, 2018.

[16] G.H. Felix Book, Holger Knauss, Carsten Demberger, Florian Mutter, "Phosphorous doping from APCVD deposited PSG, in: in Proceeding of the 34th European Photovoltaic Solar Energy Conference and Exhibition, Hamburg, Germany, 2016, pp. 2–5.

[17] M. Heilig, J. Engelhardt, G. Hahn, B. Terheiden, Comparison of laser-doped emitters from as-deposited and thermally diffused APCVD doping glasses on silicon substrates, AIP Conf. Proc. 2147 (August) (2019), https://doi.org/10.1063/1.5123865.

[18] B. Kafle, B.S. Goraya, S. Mack, F. Feldmann, S. Nold, J. Rentsch, TOPCon – technology options for cost efficient industrial manufacturing, Sol. Energy Mater. Sol. Cells 227 (2021), 111100, https://doi.org/10.1016/j.solmat.2021.111100. February.

[19] K. Ryu, C.J. Choi, H. Park, D. Kim, A. Rohatgi, Y.W. Ok, Fundamental understanding, impact, and removal of boron-rich layer on n-type silicon solar cells, Sol. Energy Mater. Sol. Cells 146 (2016) 58–62, https://doi.org/10.1016/j.solmat.2015.11.031.

[20] V.D. Mihailetchi, H. Chu, J. Lossen, R. Kopecek, Surface passivation of boron-diffused junctions by a borosilicate glass and in situ grown silicon dioxide interface layer, IEEE J. Photovoltaics 8 (2) (2018) 435–440, https://doi.org/10.1109/JPHOTOV.2018.2792422.

[21] R. Zapf-Gottwick, et al., Solar cells with laser doped boron layers from atmospheric pressure chemical vapor deposition, Sol 2 (2) (May 2022) 274–292, https://doi.org/10.3390/SOLAR2020015, 2022, Vol. 2, Pages 274-292.

[22] G. Galbiati, H. Chu, V.D. Mihailetchi, J. Libal, R. Kopecek, Latest Results in Screen-Printed IBC-ZEBRA Solar Cells, in: IEEE 7th World Conf. Photovolt. Energy Conversion, WCPEC 2018 - A Jt. Conf. 45th IEEE PVSC, 28th PVSEC 34th EU PVSEC, 2018, pp. 1540–1543, https://doi.org/10.1109/PVSC.2018.8547357, 2018.

[23] M. Juhl, C. Chan, M.D. Abbott, T. Trupke, Anomalously high lifetimes measured by quasi-steady-state photoconductance in advanced solar cell structures, Appl. Phys. Lett. 103 (24) (2013), https://doi.org/10.1063/1.4840337.

[24] B.E. Deal, M. Sklar, Thermal oxidation of heavily doped silicon, J. Electrochem. Soc. 112 (4) (1965) 430, https://doi.org/10.1149/1.2423562.

[25] D.M. Brown, P.R. Kennicott, Glass source diffusion in Si and SiO[sub 2], J. Electrochem. Soc. 118 (2) (1971) 293, https://doi.org/10.1149/1.2408020.

[26] B. Singha, C.S. Solanki, Impact of boron rich layer on performance degradation in boric acid diffused emitters for n-type crystalline Si solar cells, Mater. Res. Express 5 (1) (Jan. 2018), https://doi.org/10.1088/2053-1591/AAA2B6.

[27] J.S. Christenserr, H.H. Radamson, A.Y. Kuznetsov, B.G. Svensson, Phosphorus and boron diffusion in silicon under equilibrium conditions, Appl. Phys. Lett. 82 (14) (2003) 2254–2256, https://doi.org/10.1063/1.1566464.

[28] Chu and Haifeng, Interdigitated back contact silicon solar cells : metallisation and reverse bias characteristics, Accessed: Oct. 31, 2022. [Online]. Available: https://kops.uni-konstanz.de/handle/123456789/45903, 2019.

[29] P. Engelhart, N.P. Harder, R. Grischke, A. Merkle, R. Meyer, R. Brendel, Laser structuring for back junction silicon solar cells, Prog. Photovoltaics Res. Appl. 15 (3) (May 2007) 237–243, https://doi.org/10.1002/pip.732.

[30] F. James, E.J.F. Shackelford, W. Alexander, Mater. Sci. Eng. Handb. 232 (2001).

[31] G.A.C.M. Spierings, Wet chemical etching of silicate glasses in hydrofluoric acid based solutions, J. Mater. Sci. 28 (23) (1993) 6261–6273, https://doi.org/10.1007/BF01352182.

[32] Etching of oxides, Electrochem. Silicon Its Oxide (Dec. 2004) 131–165, https://doi.org/10.1007/0-306-47921-4_4.

[33] B. Mojrová, et al., A comparison study of boron emitter passivation by silicon oxide and a PECVD silicon nitride stack, Energy Proc. 124 (2017) 288–294, https://doi.org/10.1016/j.egypro.2017.09.301.

[34] B.E. Deal, M. Sklar, Thermal oxidation of heavily doped silicon, J. Electrochem. Soc. 112 (4) (1965) 430, https://doi.org/10.1149/1.2423562.

[35] K.R. McIntosh, P.P. Altermatt, A freeware 1D emitter model for silicon solar cells, Conf. Rec. IEEE Photovolt. Spec. Conf. 1 (x) (2010) 2188–2193, https://doi.org/10.1109/PVSC.2010.5616124.

[36] S. Duttagupta, F.J. Ma, B. Hoex, A.G. Aberle, Extremely low surface recombination velocities on heavily doped planar and textured p+ silicon using low-temperature positively-charged PECVD SiOx/SiNx dielectric stacks with optimised antireflective properties, Conf. Rec. IEEE Photovolt. Spec. Conf. (2013) 1776–1780, https://doi.org/10.1109/PVSC.2013.6744487.